Received: 17 December 2025 | Revised: 30 June 2026 | Accepted: 19 August 2026 | Published online: 16 September 2026

RESEARCH ARTICLE

Journal of Optics and Photonics Research
2026, Vol. 00(00) 1–12
DOI: 10.47852/bonviewJOPR62028826

BON VIEW PUBLISHING

# Numerical Optimization of a Divergence-Beam Surface Plasmon Resonance Sensor with $CaF_2$/ZnO/Ag/ZnTe Multilayers for Alpha-Fetoprotein-Associated Refractive Index Sensing

**Jordan H. Hossea[1,*], Athuman Mfinanga[1] and Vitalis Mwinyi[2]**

[1] *Department of Electronics and Telecommunications Engineering, Dar es Salaam Institute of Technology, United Republic of Tanzania*

[2] *Department of Legal and Industrial Metrology, College of Business Education, United Republic of Tanzania*

**Abstract:** This study presents a numerical investigation of a five-layer surface plasmon resonance (SPR) sensor employing a $CaF_2$/ZnO/Ag/ZnTe configuration, optimized through the transfer matrix method at an excitation wavelength of 633 nm. The primary objective is to numerically maximize angular refractive index (RI) sensitivity relevant to alpha-fetoprotein (AFP)-associated RI sensing. Unlike conventional SPR configurations, the proposed structure employs a sub-conventional silver film thickness of 40 nm combined with a 4 nm ZnTe protective/field-enhancing capping layer and a 6 nm ZnO adhesion layer. A rigorous theoretical analysis shows that, within the ZnO/ZnTe multilayer environment, 40 nm is the optimum Ag thickness that simultaneously minimizes ohmic losses and maximizes radiative coupling efficiency, rather than the conventional 50 nm associated with single-layer configurations. The simulation predicts a maximum angular sensitivity of 575.715°/RIU (RI unit), a figure of merit (FOM) of 125 $RIU^{-1}$, and a theoretical digitization-limited resolution of $3.55 \times 10^{-10}$ RIU (an ideal lower bound under noise-free conditions) using a 3648-pixel charge-coupled device detector with a 12-bit analog to digital converter. The modeled RI range (1.3300–1.3353) corresponds to AFP concentrations of 0–125 ng/mL, following established bulk RI calibration references. A divergence-beam (Powell lens) interrogation system eliminates mechanical scanning by capturing all angles simultaneously. The sensor numerically indicates strong potential for high RI sensitivity in the AFP-relevant range; experimental validation with functionalized surfaces and noise characterization is required to establish real-world performance.

**Keywords:** surface plasmon resonance, Powell lens, divergence beam, alpha-fetoprotein, hepatocellular carcinoma

## 1. Introduction

Alpha-fetoprotein (AFP) is a serum biomarker for hepatocellular carcinoma (HCC), the predominant form of primary liver cancer, which accounts for 70–85% of reported cases worldwide [1–3]. AFP is a glycoprotein generated in the liver during embryonic development [1], and elevated serum AFP concentrations signify the severity of chronic liver inflammation, regeneration, cirrhosis, and malignancy [3, 4]. The WHO ranks liver cancer as the sixth most prevalent malignancy and third leading cause of cancer-related mortality; in Tanzania, it ranks third among cancer-related mortality, accounting for 11.3% and 5.1% of cancer fatalities in males and females, respectively [5]. The clinically significant AFP threshold for early-stage HCC detection is approximately 25 ng/mL, a level at which many available biomedical instruments show inadequate sensitivity [1, 6].

Traditional HCC diagnostics include ultrasound, computed tomography (CT), electrochemiluminescence immunoassay (ECLIA), enzyme-linked immunosorbent assay (ELISA), and fluorescence immunoassay [7–9]. These methods offer weak sensitivity below 25 ng/mL, have long processing times, and require labeling agents. Surface plasmon resonance (SPR) biosensing is a label-free alternative with high sensitivity, fast response, and real-time capability suitable for low HCC concentrations [1, 10, 11]. SPR occurs when incident evanescent waves couple into surface plasmon polaritons (SPPs) at a metal/dielectric interface, producing a sharp resonance angle exquisitely sensitive to the refractive index (RI) of the adjacent medium, making SPR a powerful tool

***Corresponding author:** Jordan H. Hossea, Department of Electronics and Telecommunications Engineering, Dar es Salaam Institute of Technology, United Republic of Tanzania. Email: jordan.hossea@dit.ac.tz

for detecting low-level biomarker proteins that induce minor RI perturbations.

This phenomenon enables direct monitoring of biomarker surface interactions at extremely low concentrations [1, 10, 11]. Resonance occurs when the evanescent wave's horizontal propagation constant matches that of the surface plasmon wave; hence, the resonance position depends on the RI of metal, prism, and sample. Only metals with a high real-to-imaginary permittivity ratio efficiently excite SPR – silver (Ag) outperforms gold (Au) in this regard, though Au is often chosen for corrosion resistance despite its broader full-width at half-maximum (FWHM) and reduced detection accuracy [1]. Recent designs therefore add a protective overlayer atop Ag to prevent oxidation while enhancing performance [12–14].

Advanced photonic approaches such as metasurface-based biosensors and band-folding mechanisms have shown remarkable capabilities for cancer cell detection and sub-terahertz phenotyping [15]. Nevertheless, angle-interrogated SPR systems retain practical advantages in cost, compactness, and biochemical versatility.

SPR supports real-time, label-free AFP quantification with minimal sample volume [10, 11]. Owing to its high accuracy, reliability, and sensitivity to minute RI changes, SPR has been widely applied to DNA hybridization [12, 13], glucose sensing [16], formalin detection in food [17, 18], and pathogen detection including dengue, malaria, chikungunya, and cancer [19].

Multiple multilayer SPR configurations have been numerically investigated for AFP detection. Srivastava et al. [20] reported a $CaF_2/Ag/Si_3N_4/Ni/BP$ structure achieving 403.92°/RIU with a 45 nm Ag film at 633 nm, while Bahador and Aliakbari [1] built a six-layer BK7/Al/Ni/Si/BP sensor with 480°/RIU sensitivity using 38 nm Al at 633 nm. Vasimalla et al. [11] proposed a BK7/Ag/ZnTe/SiC/BP structure (Ag = 50 nm) reaching 480.46°/RIU at 633 nm, and a $CaF_2/Ag/TiO_2/PbTiO_3$ design achieved 486°/RIU with 54 nm Ag at 1000 nm [21], although the latter's use of invisible light and expensive detectors is impractical. Collectively, these motivate further optimization of Kretschmann-configuration SPR sensors in the visible regime.

Many existing SPR biosensors for AFP at 25 ng/mL suffer from inadequate sensitivity and resolution. Low sensitivity typically arises from high-index prisms such as BK7 or from Ag thicknesses in the 45–55 nm range [22]. At 45–55 nm in multilayer designs, the effective sensor thickness grows, attenuating the evanescent wave and weakening its interaction with the surface plasmon. Although 45–55 nm balances radiative and intrinsic damping in single-layer sensors, multilayer designs require reoptimization: our analysis indicates Ag should lie below 45 nm (but not below 30 nm) to preserve strong mode confinement while reducing ohmic loss [22].

Low resolution stems from mechanical-scanning implementations limited by the stepper motor's 0.001° step [23]. The proposed biosensor uses a Powell-lens-produced diverged beam that ensures uniform angular distribution and eliminates mechanical rotation. Its resolution is instead set by charge-coupled device (CCD) pixel count, analog to digital converter (ADC) bit depth, and sensor sensitivity. With a 3648-pixel CCD and 12-bit ADC, the theoretical digitization-limited angular resolution is finer than conventional motor-driven scanning though it remains an ideal lower bound achievable only under noise-free conditions. For an RI range of 1.3300–1.3353 [1] and $\Delta\theta_{res} = 3°$, the resulting angular resolution is far smaller than that of mechanical scanning [24, 25].

Prior studies have proposed adhesion materials between prism and Ag. Zinc oxide (ZnO) provides good adhesion and, unlike Cr or Ti, can be deposited in larger thicknesses without degrading performance, since Cr/Ti have complex refractive indices that lower sensitivity by broadening the resonance curve [26, 27]. Their required thinness also increases interface roughness [28]. ZnO has a purely real, high RI, supporting charge transfer without visible-light absorption; larger ZnO thicknesses also facilitate smooth deposition of Au or Ag [26, 27].

Zinc telluride (ZnTe) is a semiconductor exhibiting pronounced SPR effects owing to its high RI [29, 30]. Combining optimized Ag thickness with ZnTe roughly doubles SPR sensitivity relative to conventional designs, and ZnTe's chemical stability provides substantial protection against Ag oxidation.

In summary, reliance on Ag thicknesses of 45–55 nm is a major limitation of traditional multilayer SPR sensors that range suited single-layer configurations balancing radiative and ohmic damping, but adhesion/protective dielectric overlayers alter the boundary conditions and effective optical path, shifting the optimum. Additionally, motor-driven angular scanning limits resolution to the 0.001° step [23]. This study addresses these limitations by (i) systematic transfer matrix method (TMM)-based optimization of a $CaF_2$/ZnO/Ag/ZnTe multilayer at 633 nm, showing via loss-balance analysis that 40 nm is optimal in this multilayer context; (ii) implementing a divergence-beam (Powell-lens) interrogation with a 3648-pixel CCD that eliminates mechanical scanning; (iii) evaluating sensitivity, FWHM, FOM, detection accuracy, and theoretical digitization limited resolution (TDLR) across the AFP-relevant RI range; and (iv) numerical robustness analysis quantifying sensitivity to fabrication tolerances. All results are purely numerical—no experimental fabrication, functionalization, or biological measurements were performed.

## 2. Methodology

### 2.1. Theoretical model

Figure 1 shows the proposed SPR sensor comprises five layers in the Kretschmann configuration, namely, (1) $CaF_2$ prism (RI = 1.43290 at 633 nm [31])), (2) ZnO adhesion layer, (3) Ag plasmonic film, (4) ZnTe protective/field-enhancing layer, and (5) aqueous sensing medium. All simulations use $\lambda = 633$ nm with the optical constants in Table 1. Sensing-medium RI spans $n_s = 1.3300$ (deionized water) to 1.3353, corresponding to AFP concentrations of 0–125 ng/mL from the bulk RI calibration of Bahador and Aliakbari [1], as summarized in Table 2, where progressive AFP addition yields cumulative $\Delta n = 0.0053$ over 0–125 ng/mL. Practical SPR-based AFP sensing would additionally require surface functionalization (e.g., anti-AFP antibody immobilization) to capture binding-induced local RI changes; the present study models bulk-RI sensing only and does not include binding kinetics or surface bio-recognition layers.

It is assumed that the reflected diverged beam is captured by the CCD sensor (TCD1304AP) 8-bits controlled by ATmega1284 with12-bits ADC of the controller, respectively. The number of pixels of 3648 pixels imbedded to the microcontroller, which has 12-bit ADC converter. Finally, the last layer is the sensing medium, ranging from the pure water with RI of $n_s = 1.33$ to 1.3353 depending on the AFP concentration, which varies 0 to 125 ng/ml, respectively, as shown in Table 2 [1].

**Figure 1**
**Schematic diagram of the designed SPR biosensor**

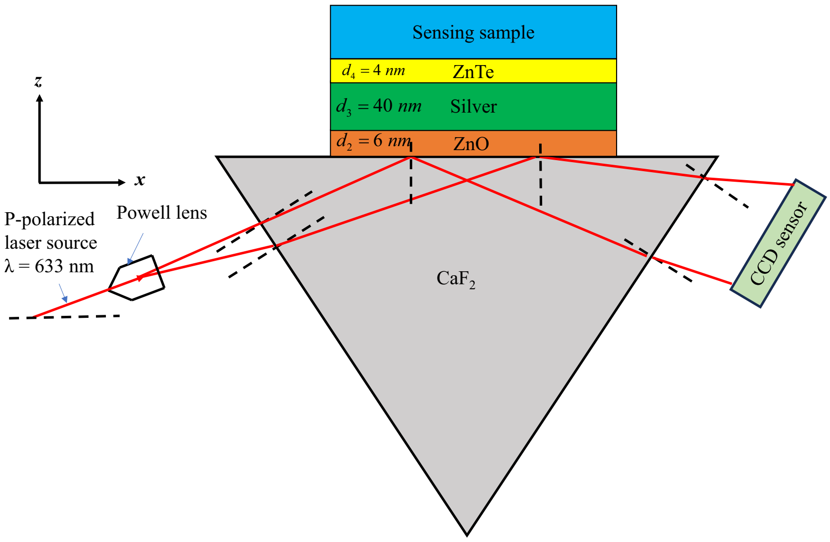


**Table 1**
**Optical parameters used in the TMM simulation (at Wavelength $\lambda$ = 633 nm)**

| Layer | Material | Refractive index ($n$) | Reference |
|---|---|---|---|
| Prism | $CaF_2$ | 1.43290 | [31] |
| Adhesion | ZnO | 1.9800 | [32] |
| Plasmonic | Ag | 0.0561 + 4.2760i | [33] |
| Protective | ZnTe | 2.9887 | [34] |
| Medium (water) | $H_2O$ | 1.3300 | – |

**Table 2**
**Modeled bulk RI of AFP-containing medium at different concentrations**

| S. No | Alpha-fetoprotein (AFP) concentration (ng/mL) | AFP associated RI [1] |
|---|---|---|
| 1 | 0 | 1.3300 |
| 2 | 25 | 1.3310 |
| 3 | 50 | 1.3321 |
| 4 | 75 | 1.3332 |
| 5 | 100 | 1.3343 |
| 6 | 125 | 1.3353 |

## 2.2. Reflectance computation for the multilayers

The matrix method is the simple method for computing electromagnetic fields in multilayer with high accuracy [32]. The first layer P-polarized field (P) for the electric and magnetic fields $E^0_{x1}$ and $H^0_{y1}$ and last layer $E^0_{x4}$ and $H^0_{y4}$ were related by Equation (1).

$$\begin{bmatrix} H^0_{y1} \\ -E^0_{x1} \end{bmatrix} = M_{ij} \begin{bmatrix} H^0_{y4} \\ -E^0_{x4} \end{bmatrix}, \tag{1}$$

Equations (2), (3), and (4) computes evanescent wave along $x$-component in ZnO, Ag and ZnTe layer, respectively

$$\begin{bmatrix} H^0_{yZnO} \\ -E^0_{xZnO} \end{bmatrix} = M_{ZnO} \begin{bmatrix} H_{yZnO}(z) \\ -E_{xZnO}(z) \end{bmatrix} = \begin{pmatrix} \cos\beta_{Zn0} & -\left(\frac{i}{q_{ZnO}}\right)\sin\beta_{Zn0} \\ -iq_{ZnO}\sin\beta_{Zn0} & \cos\beta_{Zn0} \end{pmatrix} \begin{bmatrix} H_{yZnO}(z) \\ -E_{xZnO}(z) \end{bmatrix} \tag{2}$$

$$\begin{bmatrix} H^0_{yAg} \\ -E^0_{xAg} \end{bmatrix} = M_{Ag} \begin{bmatrix} H_{yAg}(z) \\ -E_{xAg}(z) \end{bmatrix} = \begin{pmatrix} \cos\beta_{Ag} & -\left(\frac{i}{q_{Ag}}\right)\sin\beta_{Ag} \\ -iq_{Ag}\sin\beta_{Ag} & \cos\beta_{Ag} \end{pmatrix} \begin{bmatrix} H_{yAg}(z) \\ -E_{xAg}(z) \end{bmatrix} \tag{3}$$

$$\begin{bmatrix} H^0_{yZnTe} \\ -E^0_{xZnTe} \end{bmatrix} = M_{ZnTe} \begin{bmatrix} H_{yZnTe}(z) \\ -E_{xZnTe}(z) \end{bmatrix} = \begin{pmatrix} \cos\beta_{ZnTe} & -\left(\frac{i}{q_{ZnTe}}\right)\sin\beta_{ZnTe} \\ -iq_{ZnTe}\sin\beta_{ZnTe} & \cos\beta_{ZnTe} \end{pmatrix} \begin{bmatrix} H_{yZnTe}(z) \\ -E_{xZnTe}(z) \end{bmatrix} \tag{4}$$

$$M_{ij} = \begin{pmatrix} \cos\beta_{Zn0} & -\left(\frac{i}{q_{ZnO}}\right)\sin\beta_{Zn0} \\ -iq_{ZnO}\sin\beta_{Zn0} & \cos\beta_{Zn0} \end{pmatrix} \begin{pmatrix} \cos\beta_{Ag} & -\left(\frac{i}{q_{Ag}}\right)\sin\beta_{Ag} \\ -iq_{Ag}\sin\beta_{Ag} & \cos\beta_{Ag} \end{pmatrix} \times \begin{pmatrix} \cos\beta_{ZnTe} & -\left(\frac{i}{q_{ZnTe}}\right)\sin\beta_{ZnTe} \\ -iq_{ZnTe}\sin\beta_{ZnTe} & \cos\beta_{ZnTe} \end{pmatrix} \tag{5}$$

$$M_{ij} = \begin{pmatrix} M_{11} & M_{12} \\ M_{21} & M_{22} \end{pmatrix} \tag{6}$$

$$q_k = \frac{\left(n_k^2 - (n_p\sin\beta_i)^2\right)^{\frac{1}{2}}}{n_k^2} \tag{7}$$

$$\beta_k = \frac{2\pi d_k}{\lambda}\left(n_k^2 - n_p^2\sin^2\theta_i\right)^{\frac{1}{2}} \tag{8}$$

where $M_{ij}$ is the matrix relates the wave propagation for each layer in which $q_k$, $\beta_k$, and $d_k$ are wave impedance factor, phase shift factor, and thickness of the $k^{th}$ layer, respectively. Based on designed SPR sensor k stand for ZnO layer, silver (Ag) layer, and ZnTe layer. The total reflection coefficient for the transverse magnetic field for the wave propagation through multilayer media and is expressed by Equation (9) as follows:

$$r^{TM} = \frac{H_y^r}{H_y^i} = \frac{\left(M_{11} + M_{12}q_{sample}\right)q_1 - \left(M_{21} + M_{22}q_{sample}\right)}{\left(M_{11} + M_{12}q_{sample}\right)q_1 + \left(M_{21} + M_{22}q_{sample}\right)} \tag{9}$$

$$q_{sample} = \frac{\left(n_{sample}^2 - (n_p\sin\theta_i)^2\right)^{\frac{1}{2}}}{n_{sample}^2} \tag{10}$$

Finally, the TM reflectance power is computed by

$$R = \left|r^{TM}\right|^2 \tag{11}$$

## 2.3. Electromagnetic field distribution

The algorithm for TM wave ($H_x = H_z = 0$ and $E_y = 0$) propagation was derived by Ibrahim with multiple layers stacked vertically [32]. The algorithm computes the evanescent field distribution in prism layer and is expressed as:

$$H_{y1}(x,z,t) = H_{y1}(z)\exp\left[j\left(k_0 n_1\sin\theta_1 x - \omega t\right)\right] \tag{12}$$

$$E_{x1}(x,z,t) = E_{x1}(z)\exp\left[j\left(k_0 n_1\sin\theta_1 x - \omega t\right)\right] \tag{13}$$

$$E_{zj}(x,z,t) = E_{zj}(z)\exp\left[j\left(k_0 n_j\sin\theta_j x - \omega t\right)\right] \tag{14}$$

where by $H_{y1}(z)$, $E_{x1}(z)$, and $E_{z1}(z)$ maximum magnetic, electric fields in their appropriate direction, and $k_0 = \frac{2\pi}{\lambda}$. $H_{yj}(z)$ is the amplitude of magnetic field in $y$ - direction, $E_{xj}(z)$ and $E_{zj}(z)$, electric field amplitude $x$- and $z$-directions in $j$ layer. $\theta_j$ is the propagation angle and $k_0 = \frac{2\pi}{\lambda_0}$ the wave number in vacuum. From Snell's law $n_j\sin\theta_j = n_0\sin\theta_0$ and trigometric identity property. The magnetic and electric field propagated in ZnO, Ag, and ZnTe layer is given by Equation (15), (16), and (17), respectively:

$$\begin{bmatrix} H_{yZnO}(z) \\ -E_{xZnO}(z) \end{bmatrix} = \begin{bmatrix} \cos\left(k_0 n_{ZnO} z\cos\theta_{ZnO}\right) & \frac{i}{q_{Zn0}}\sin\left(k_0 n_{ZnO} z\cos\theta_{ZnO}\right) \\ iq_{Zn0}\sin\left(k_0 n_{ZnO} z\cos\theta_{ZnO}\right) & \cos\left(k_0 n_{ZnO} z\cos\theta_{ZnO}\right) \end{bmatrix} \begin{bmatrix} 1 + r^{TM} \\ q_{ZnO}\left(1 - r^{TM}\right) \end{bmatrix} H_y^i \tag{15}$$

$$\begin{bmatrix} H_{yAg}(z) \\ -E_{xAg}(z) \end{bmatrix} = \begin{bmatrix} \cos\left(k_0 n_{Ag}(2z - d_{ZnO})\cos\theta_{Ag}\right) & \frac{i}{q_{Ag}}\sin\left(k_0 n_{ZnTe}(2z - d_{ZnO})\cos\theta_{Ag}\right) \\ iq_{Ag}\sin\left(k_0 n_{Ag}(2z - d_{ZnO})\cos\theta_{Ag}\right) & \cos\left(k_0 n_{Ag}(2z - d_{ZnO})\cos\theta_{Ag}\right) \end{bmatrix} \times \begin{bmatrix} H_{yZnO}(z) \\ -E_{xZnO}(z) \end{bmatrix} \tag{16}$$

$$\begin{bmatrix} H_{yZnTe}(z) \\ -E_{xZnTe}(z) \end{bmatrix} = \begin{bmatrix} \cos\left(k_0 n_{ZnTe}\left(2z - (d_{ZnO} + d_{Ag})\right)\cos\theta_{ZnTe}\right) & \frac{i}{q_{ZnTe}}\sin\left(k_0 n_{ZnTe}\left(2z - (d_{ZnO} + d_{Ag})\right)\cos\theta_{ZnTe}\right) \\ iq_{ZnTe}\sin\left(k_0 n_{ZnTe}\left(2z - (d_{ZnO} + d_{Ag})\right)\cos\theta_{ZnTe}\right) & \cos\left(k_0 n_{ZnTe}\left(2z - (d_{ZnO} + d_{Ag})\right)\cos\theta_{ZnTe}\right) \end{bmatrix} \times \begin{bmatrix} H_{yAg}(z) \\ -E_{xAg}(z) \end{bmatrix} \tag{17}$$

In which $\boldsymbol{\theta_{ZnO}}$, $\boldsymbol{\theta_{Ag}}$, and $\boldsymbol{\theta_{ZnTe}}$ are the incident angle at prism/ZnO, ZnO/Ag, and Ag/ZnTe interface, respectively. $\boldsymbol{H_y^i}$ is the incident magnetic field, which was assumed as unity. Incident electric field is mathematically related to incident magnetic field $\boldsymbol{E_x^i = q_{prism} H_y^i}$, where $\boldsymbol{q_{prism}}$ is the wave impedance due to prism.

## 2.4. Performance parameters

*2.4.1. Sensitivity, FWHM, detection accuracy, and figure of merit*

Sensitivity is the specificity of the ratio of the variation of the resonance angle ($\Delta\theta_{res}$) to the RI of the measured sample ($\Delta n_s$) as expressed by Equation 18 [35, 36].The FWHM is the angular width at half of full power of the SPR reflectivity spectrum, which is computed as per Equation (19). The narrower the FWHM the better. It is primary parameter that defines two secondary parameters: detection accuracy (DA) and figure of merit (FOM). DA is another crucial metric that indicates how well the sensor can measure RI changes [35, 36]. The DA is inverse proportional to the FWHM [35, 36]. However, most of the published paper assumes that $R_{min}$ that why its formula is written as $DA = \frac{1}{FWHM}$ it is incorrect because practically $R_{min}$. The quality factor (QF) is the product of sensitivity and DA. The relation is defined of DA as Equation (20).

$$S = \frac{\Delta\theta_{res}}{\Delta n_s} \tag{18}$$

$$FWHM = \frac{1}{2}(\theta_{max} - \theta_{min}) \tag{19}$$

$$DA = \frac{1 - R_{min}}{FWHM} \tag{20}$$

$$FOM = S.DA \tag{21}$$

*2.4.2. Resolution*

The diverged-beam SPR sensor uses a linear CCD or CMOS to capture the reflected beam. Its angular resolution depends on the total pixel count covered by the beam, the ADC bit depth, and the sensor sensitivity [24, 25]. Therefore, the number of pixels covered by the reflected beam and number of bits of ADC gives the angular resolution $\sigma_s$

$$\sigma_s = \frac{\Delta\theta_{res}}{N_{pixel}} \times \frac{1 pixel}{(2^n - 1)} \tag{22}$$

where $N_{pixel}$, $n$, and $\Delta\theta_{res}$ are the CCD total pixel covered the entire reflected, number of bits of ADC converter, and shift resonance from lower concentration of AFP to the next concentration of AFP. Thus, TDLR can be calculated, as shown in Equation (23) [24]

$$\text{Resolution}\,(\sigma_{RI}) = \frac{\sigma_s}{Sensitivity}$$

$$\text{Resolution}\,(\sigma_{RI}) = \frac{\frac{\Delta\theta_{res}}{N_{pixel}} \times \frac{1 pixel}{(2^n - 1)}}{\frac{\Delta\theta_{res}}{\Delta n_s}}$$

$$\text{Resolution}\,(\sigma_{RI}) = \frac{\Delta n_s}{N_{pixel}} \times \frac{1 pixel}{(2^n - 1)} \tag{23}$$

Equation (23) defines the TDLR as the ideal lower-bound resolution under noise-free conditions with perfect digitization; the experimentally achievable resolution will exceed the TDLR and must be determined by full noise characterization including detector noise, source fluctuations, mechanical vibration, fabrication imperfections, and signal-processing uncertainty.

## 3. Results and Discussion

### 3.1. Optimizing the thickness silver film layer for single layer

The impact of Ag thickness (30–60 nm) on the SPR resonance was first evaluated in the $CaF_2$/Ag/sensing medium configuration (without ZnO or ZnTe) to establish a single-layer baseline. SPR performance depends critically on the metal film, with thickness governing plasmon excitation and damping. The resonance curves sharpen considerably from 30 to 50 nm (Figure 2): the shallow, broad dip at 30 nm reflects a radiatively damped regime with weak resonance, while beyond 50 nm

**Figure 2**
**SPR reflectivity curve at different thicknesses of Ag for single layer**

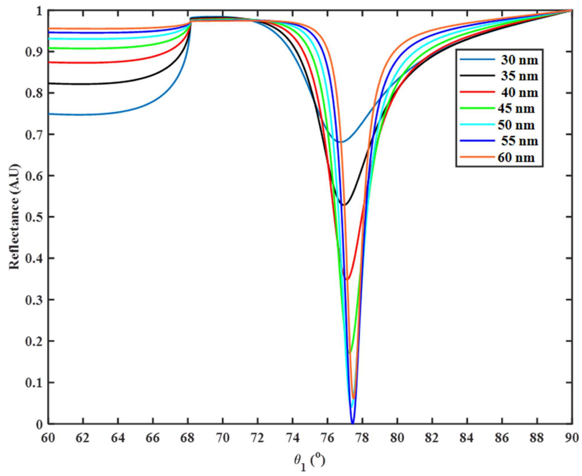


(55, 60 nm) the minimum reflectance rises again and FWHM broadens, indicating ohmic absorption dominance in thicker metal films [37, 38]. The increased absorption in the thicker metal layer dampens the plasmon resonance, producing a wider, less defined curve [22]. Thus, 50 nm is optimal in the single-layer configuration; however, in multilayer, there is optimum shifts once adhesion and protective dielectric overlayers are introduced.

Progression to a deeper dip with increasing thickness up to 50 nm signifies improved mode confinement and more efficient photon-to-plasmon coupling [22].

At 55 and 60 nm, performance degrades; the reflectance dip becomes shallower as ohmic (absorption) losses dominate thicker metal forces the field through more material, dissipating energy as heat [22]. The 50 nm film thus balances radiative and absorptive losses optimally in the single-layer case. However, when ZnO adhesion and ZnTe protective layers are added, this balance shifts; the study therefore adopts 40 nm Ag, which improves energy coupling and sensitivity in the multilayer stack.

### 3.2. Electric field enhancement the thickness silver film layer

Figure 3 shows the $x$-component of the electric field through a single Ag layer of varying thickness. At 35 nm, strong radiative damping poorly confines the plasmon and the evanescent field leaks into the prism, reducing sensitivity. At 45–55 nm, light couples efficiently into the SPP mode and the field is strongly enhanced at the Ag/analyte interface. At 60 nm, the evanescent field decays within the Ag before reaching the opposite interface, localizing the SPP at the prism/metal side and reducing analyte interaction. Although Ag has lower ohmic loss than Au in the visible, thicker Ag still increases attenuation and shortens the effective interaction volume

### 3.3. Optimizing of ZnO adhesion layer

Table 3 and Figure 4 indicate that, when the ZnO thickness is increased in 2 nm steps, the sensitivity increases only marginally by 2°/RIU per step, which suggests that ZnO primarily acts as an adhesion layer and does not substantially enhance sensitivity. The minimum reflectance dip nevertheless reduces by 0.02 per 2 nm increase in ZnO thickness, which indicates progressively improved

**Figure 3**
**Electric field enhancement in x-component at different thicknesses of Ag for single layer**

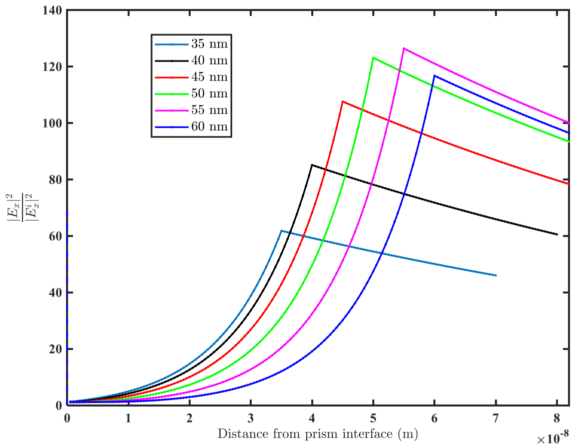


**Figure 4**
**SPR reflectivity curve at different ZnO thicknesses**

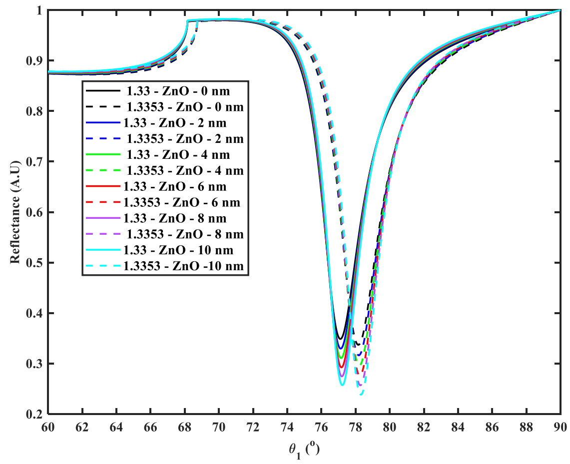


optical energy coupling. A ZnO thickness of 6 nm was selected as a balance between adequate adhesion, smooth Ag deposition, and improved energy coupling.

### 3.4. Combined ZnO/Ag/ZnTe optimization and sensitivity

Figure 5(a)–(d) shows SPR reflectance curves for four Ag thicknesses (40, 45, 50, and 55 nm), each combined with ZnTe of 0, 2, or 4 nm, with ZnO fixed at 6 nm. The results confirm Section 3.3: the ZnTe cap progressively sharpens and deepens the dip for 40 nm Ag (Figure 5(a)), approaching near-critical coupling at ZnTe = 4 nm. For thicker Ag (50 and 55 nm), increasing ZnTe to 4 nm degrades performance (higher R_min, lower S) since these configurations are already over-damped and additional dielectric redistribution further suppresses radiative coupling.

For 40 nm Ag combined with 0, 2, and 4 nm ZnTe, the resonance shifts are 1.08°, 1.42°, and 3.00°, respectively, the corresponding minimum dips are 0.28415, 0.22110, and 0.06815, and the resulting sensitivities are 203.77, 267.92, and 566.04°/RIU. For 45 nm Ag, the shifts (1.12°, 1.52°, and 1.76°) and sensitivities (211.32, 286.79, and 332.08°/RIU) follow a similar but weaker trend. For 50 nm Ag, the 4 nm ZnTe configuration is clearly over-damped (sensitivity drops to 96.23°/RIU) and for 55 nm Ag, the sensitivity at 4 nm ZnTe falls to 52.83°/RIU. These results indicate that the highest sensitivity in the multilayer system is achieved at Ag = 40 nm with ZnTe = 4 nm, where an optical coupling efficiency of 93.19% is reached.

For 45 nm Ag (Figure 5(b)), ZnTe = 0, 2, and 4 nm yields resonance shifts of 1.12°, 1.52°, and 1.76°, minimum dips of 0.11605, 0.06325, and 0.3105 and sensitivities of 211.32, 286.79, and 332.08°/RIU ($\Delta n$ = 0.0053). The 2 nm ZnTe gives the deepest dip. Sensor improvement stems from ZnTe's high RI (2.9881) acting as a field-enhancing cap that concentrates the evanescent field at the sensing interface [39].

For 50 nm Ag (Figure 5(c)), ZnTe = 0, 2, 4 nm gives resonance shifts of 1.15°, 1.61°, and 0.51°, minimum dips of 0.01435, $1.29 \times 10^{-3}$ and 0.51035, and sensitivities of 216.98, 304.77, and 96.23°/RIU.

For 55 nm Ag (Figure 5(d)), ZnTe = 0, 2, 4 nm yields shift of 1.17°, 1.67°, and 0.28°, minimum dips of 0.01245, 0.05285, and 0.69035 and sensitivities of 220.75, 315.09, and 52.83°/RIU. Although 55 nm Ag provides better field confinement, ohmic losses grow; its maximum sensitivity (315.09°/RIU) exceeds that of 50 nm (304.77°/RIU) but is surpassed by the 45 nm/4 nm ZnTe combination (332.08°/RIU). Overall, the highest sensitivity is obtained at Ag = 40 nm and ZnTe = 4 nm (566.04°/RIU) with an average minimum dip of 0.06815 and optical coupling efficiency of 93.19%.

Adding a 2 nm ZnTe layer sharply narrows the SPR dip and deepens R_min. The high-RI ZnTe (RI = 2.9881) reconcentrates the electromagnetic field at the external interface, enhancing analyte interaction and mitigating field loss in adjacent layers [40]. This yields a sharper plasmon resonance with narrower FWHM

**Table 3**
**Variation of sensitivity and average minimum dip at different ZnO thickness**

| S. No | Thickness of ZnO($nm$) | Resonance shift($\Delta\theta_{res}$) | Sensitivity $S = \frac{\Delta\theta_{res}}{\Delta n_s}\left(\frac{°}{RIU}\right)$ | Average minimum dip($R_{min}$()) | Energy coupling efficiency (%) |
|---|---|---|---|---|---|
| 1 | 0 | 1.05 | 198 | 0.34 | 66 |
| 2 | 2 | 1.06 | 200 | 0.32 | 68 |
| 3 | 4 | 1.07 | 202 | 0.3 | 70 |
| 4 | 6 | 1.08 | 204 | 0.28 | 72 |
| 5 | 8 | 1.08 | 204 | 0.27 | 73 |
| 6 | 10 | 1.09 | 206 | 0.25 | 75 |

**Figure 5**
**SPR reflectivity curve at different thicknesses of ZnTe**

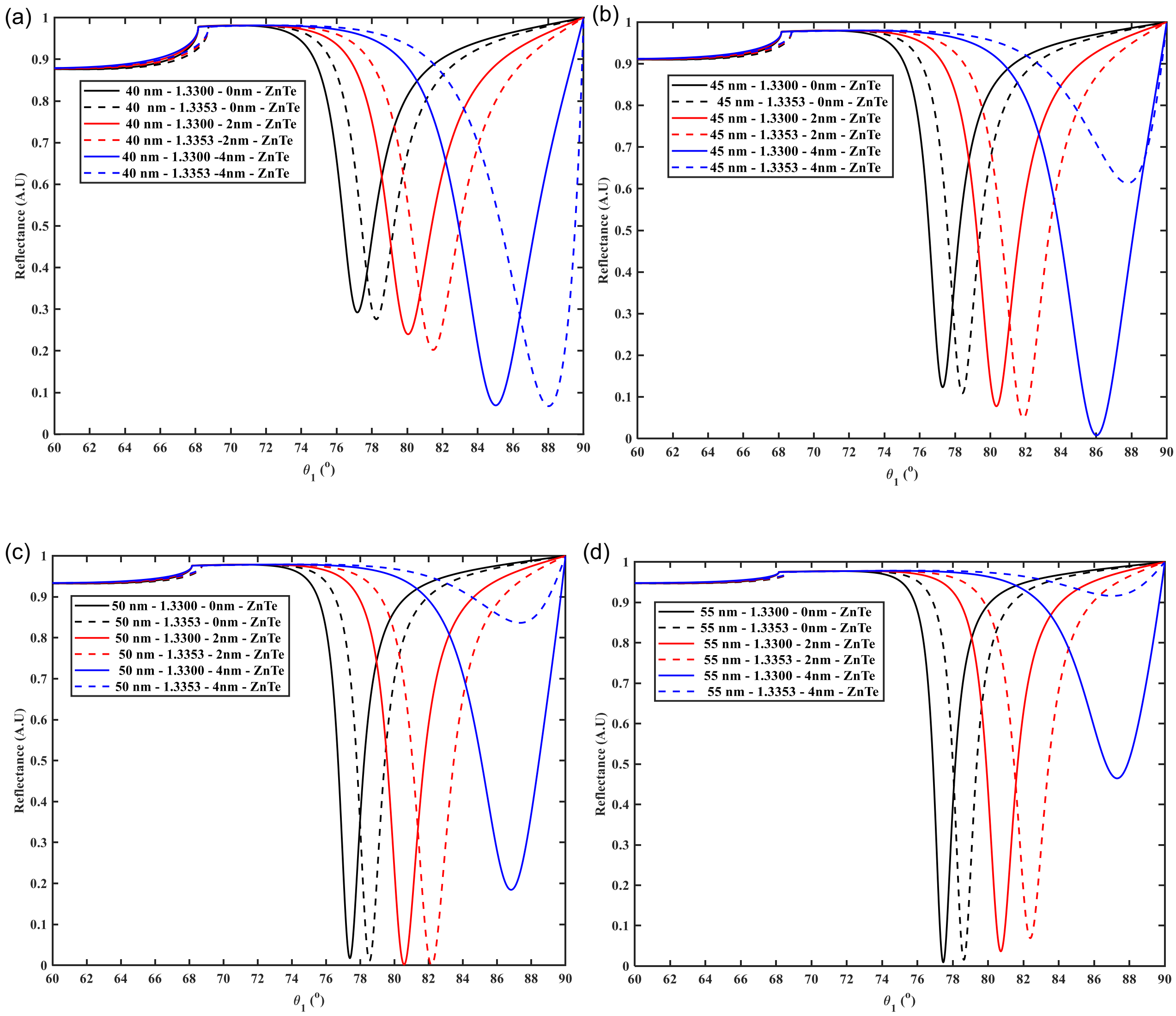


and deeper minimum dip compensating for the suboptimal performance of the 40 nm Ag layer alone [40].

## 3.5. Electric field distribution in each layer ZnO/Ag/ZnTe

Figure 6 shows the $x$-component of the electric field ($|E_x|$) for Ag thicknesses of 40, 45, 50, and 55 nm combined with ZnTe of 0, 2, or 4 nm (ZnO = 6 nm). By continuity of $E_x$ across boundaries, this component interacts with the surface plasmon wave along the sample/Ag interface. The normalized $|E_x|$ curves (Equation 17) show a peak of 930.6 at Ag = 40 nm versus 53.5 at Ag = 55 nm about a 17× enhancement. When Ag decreases to 35 nm, $|E_x|$ drops to 468.4, indicating that field enhancement degrades on either side of the 40 nm optimum. These results confirm that in a multilayer SPR sensor with adhesion and capping layers, the Ag thickness must be reoptimized relative to the single layer 45–55 nm range.

**Figure 6**
**Electric field distribution curve at different thicknesses of Ag**

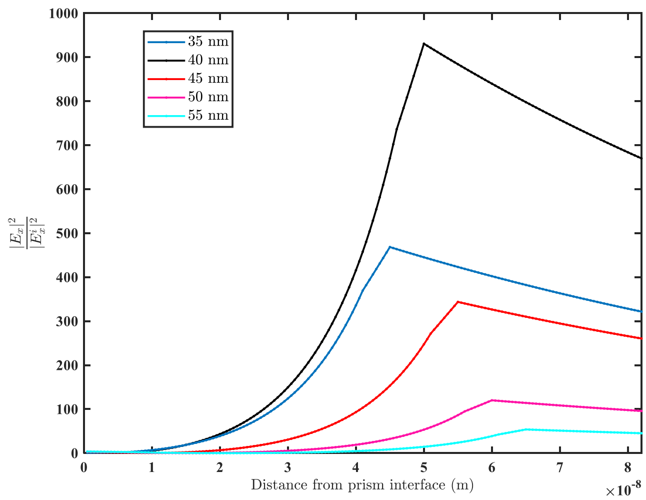

### 3.6. The application and performance of designed SPR biosensor in detection AFP-associated RI

#### *3.6.1. SPR biosensor reflectivity of AFP-associated RI at different concentrations*

Figure 7 shows simulated SPR reflectance curves for the modeled AFP concentrations. At 0, 25, and 120 ng/mL the minimum dip is approximately 0.09 arbitrary unit (a.u.); at 50, 75, and 100 ng/mL it approaches zero, indicating highly efficient photon-to-plasmon coupling and easy resonance identification. A clear resonance-angle shift accompanies each 25 ng/mL increment, indicating that the proposed configuration resolves small AFP-induced RI variations, while the FWHM remains approximately constant.

**Figure 7**
**SPR reflectance curves at different concentrations of AFP**

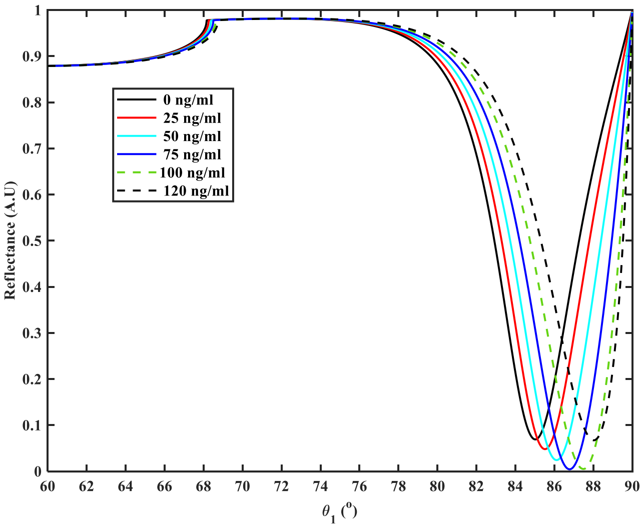


#### *3.6.2. Sensitivity and FWHM*

Figure 8 indicates sensitivity increases from 500 to 574.42° /RIU as concentration increases from 25 to 100 ng/mL and then slightly decreases to 566.04°/RIU at 125 ng/mL. This indicates that the sensor is most sensitive in the range of 75–100 ng/mL. When AFP concentration is less than 75 ng/mL, the sensitivity is low.

FWHM initially rises from 4.55° to 4.72° as concentration increases from 0 to 75 ng/mL, then falls to 4.38° at 125 ng/mL. Narrower FWHM enables more precise resonance-angle detection; the narrowest FWHM is 4.38° at 125 ng/mL, within acceptable limits and somewhat lower than several existing works.

**Figure 8**
**Sensitivity and FWHM at different AFP concentrations (ng/mL)**

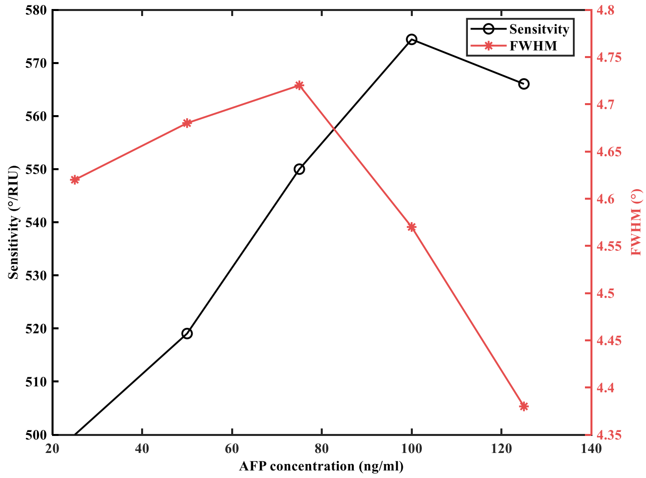


$R_{min}$ is the minimum reflectivity at the resonance angle; an ideal SPR sensor drives $R_{min}$ toward 0 for perfect coupling into the surface plasmon. $R_{min}$ decreases from 0.0691 to 0.0044 at 75 ng/mL, then rises to 0.0672 at 125 ng/mL, giving the most efficient coupling at 75 ng/mL and 100 ng/mL ($R_{min}$ = 0.0050) (Table 4). Energy coupling efficiency, $(1 - R_{min}) \times 100\%$, exceeds 93% for all concentrations and peaks at 99.56% at 75 ng/mL. Thus, the proposed SPR converts photon-to-plasmonic energy with up to ~99.56% efficiency, simplifying the resonance-angle localization algorithm across all AFP concentrations.

#### *3.6.3. Regression analysis for computing overall sensitivity of SPR sensor*

Figure 9 shows correlation coefficients $R^2$ of 0.9992 and 0.9982 for modeled bulk RI of AFP and AFP concentration in relation to resonance angle. Because $R^2$ is close to unity implies that modeled bulk RI of AFP and AFP concentration is linearly related to resonance angle with the regression equation of $\theta_{res} = 575.715n_s - 680.737$ and $\theta_{res} = 0.0245C(\text{ng/mL}) + 84.9486$. These linear equation gives bulk sensitivity in terms of modeled bulk RI of AFP and AFP concentration of $\frac{\partial\theta_{res}}{\partial n_s} = \frac{575.7154^\circ}{RIU}$ and $\frac{\partial\theta_{res}}{\partial C} = \frac{0.0247^\circ}{\frac{ng}{mL}}$, respectively, which are computed from the slope of the regression linear equation. Therefore, an overall sensitivity of the proposed SPR sensor is 575.72 °/RIU.

#### *3.6.4. Detection accuracy and figure of merits*

Figure 10 shows DA increases from 0.205 to 0.218/° as concentration rises from 0 to 100 ng/mL, then decreases slightly to

**Table 4**
**SPR biosensor performance at different AFP concentrations**

| AFP concentration (ng/ml) | RI | $\theta_{res}$ (°) | $\Delta\theta_{res}$ (°) | Sensitivity $\left(\frac{\circ}{RIU}\right)$ | $R_{min}$ | $(1-R_{min})$ | FWHM(°) |
|---|---|---|---|---|---|---|---|
| 0 | 1.3300 | 85.02 | – | – | 0.0691 | 0.9309 | 4.55 |
| 25 | 1.3310 | 85.52 | 0.50 | 500.00 | 0.0481 | 0.9519 | 4.62 |
| 50 | 1.3321 | 86.11 | 1.09 | 519.05 | 0.0243 | 0.9757 | 4.68 |
| 75 | 1.3332 | 86.78 | 1.76 | 550.00 | 0.0044 | 0.9956 | 4.72 |
| 100 | 1.3343 | 87.49 | 2.47 | 574.42 | 0.0050 | 0.9950 | 4.57 |
| 125 | 1.3353 | 88.02 | 3.00 | 566.04 | 0.0672 | 0.9328 | 4.38 |

**Figure 9**
**Linear regression fit of resonance angle against (a) modeled bulk AFP RI and (b) AFP concentration (ng/mL)**

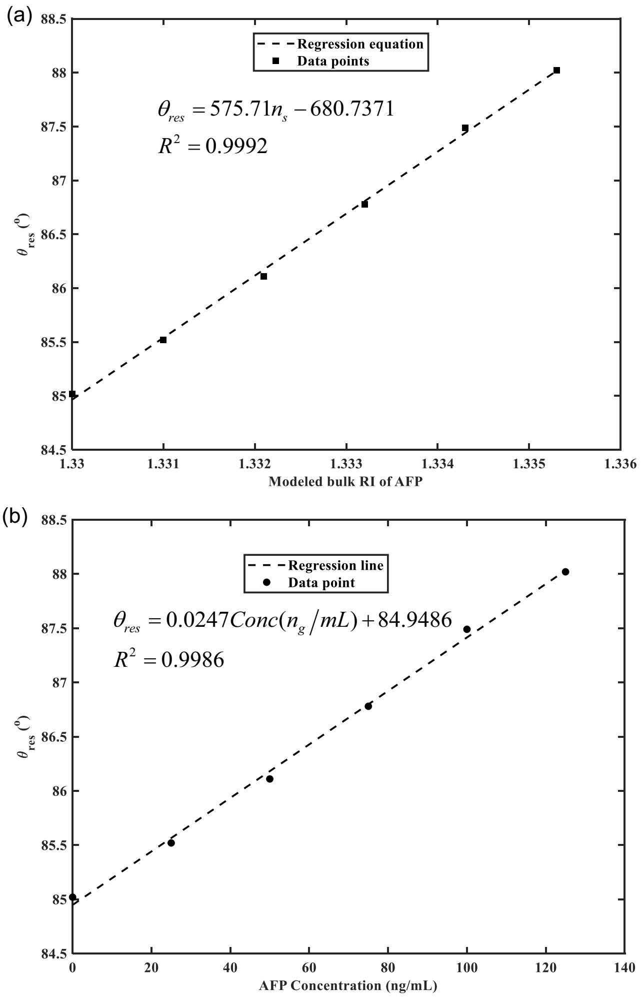


0.213 at 125 ng/mL; higher DA is better, giving the best DA at 100 ng/mL. FOM (= S × DA) represents overall performance excluding detector resolution, rising from 103 to 125.22 as concentration increases from 25 to 100 ng/mL and then decreasing to 120.57 at 125 ng/mL. The highest FOM is at 100 ng/mL.

#### *3.6.5. Theoretical digitization limited resolution of SPR sensor*

Table 5 lists the TDLR at each modeled AFP concentration. TDLR remains essentially constant at $3.55 \times 10^{-10}$ RIU across all concentrations because $\Delta\theta_{res}$ and $N\_pix \times 2^n$ are fixed system parameters and sensitivity varies by <15%. TDLR is an ideal theoretical lower bound under noise-free conditions with perfect digitization it should not be interpreted as an achievable system resolution. A realistic value requires full experimental noise characterization (CCD dark current, shot noise, source drift, mechanical vibration, fabrication tolerance, and signal-processing uncertainty) and is expected to be one or more orders of magnitude higher. The small TDLR is a consequence of the divergence-beam architecture, which captures the entire angular fan without mechanical rotation and is not constrained by the 0.001° step of a stepper motor.

**Figure 10**
**FOM and DA at different AFP concentrations (ng/mL)**

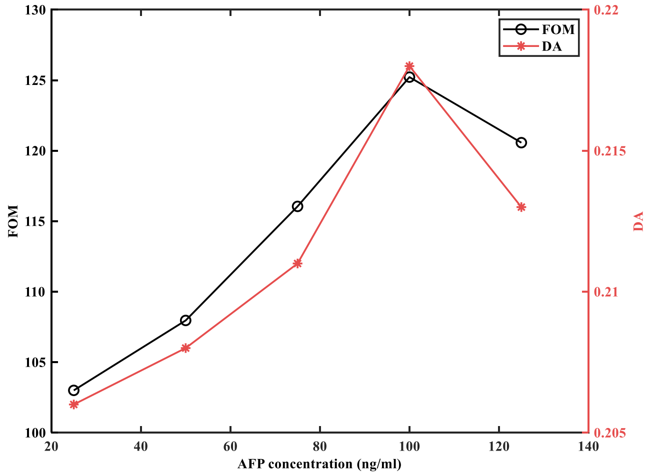


### 3.7. Robustness and sensitivity analysis

A numerical robustness analysis perturbed key structural parameters within realistic fabrication tolerances. Table 6 summarizes sensitivity variation under ±2 nm perturbations of Ag and ZnO thickness, ±1 nm of ZnTe, and ±5% in the imaginary part of the Ag RI. Key findings; (i) sensitivity is moderately sensitive to ±2 nm variation in Ag thickness (≈12–15%), which is feasible with DC magnetron sputtering that routinely achieves sub-nanometre control; (ii) ZnO thickness has negligible impact (<1%), consistent with its adhesion only role; (iii) ZnTe thickness is the most sensitive parameter, with +1 nm over-deposition reducing sensitivity by ~45%, indicating that atomic-layer deposition (ALD) with sub-nanometre control is recommended; and (iv) ±5% perturbation in the optical constants (typical measurement uncertainty) produces only ≈1.8% change, indicating robustness to material-property uncertainty.

### 3.8. A comparative analysis of the proposed with a recently published paper

Table 7 compares the proposed sensor with recently published numerical SPR biosensors targeting AFP or HCC biomarkers. All compared structures are purely numerical simulations; no experimental measurements are included, and sensitivity values are compared at the same wavelength (633 nm) where possible. Within comparable Kretschmann configuration angular interrogation SPR sensors at 633 nm, the proposed structure achieves the highest reported numerical sensitivity (575.72°/RIU) roughly a 20% improvement over the next best comparable result (480.46°/RIU; [1]). Direct sensitivity comparison across studies must nevertheless account for differences in prism, metal, operating wavelength, and RI sensing range.

### 3.9. Steps to experimental validation

Since the present results are purely numerical, experimental validation is required before any clinical or analytical claims. A realistic validation programme should include (i) deposition of the $CaF_2$/ZnO/Ag/ZnTe stack by RF sputtering (ZnO), DC magnetron sputtering (Ag) and atomic layer deposition (ZnTe), with in situ thickness monitoring within Table 6 tolerances; (ii) surface and optical characterization via AFM (roughness),

**Table 5**
**Theoretical digitization-limited resolution at each AFP concentration (3648-pixel CCD, 12-bit ADC)**

| AFP concentration (ng/mL) | RI | DA | FOM | Resolution ($\times 10^{-10}$ RIU) |
|---|---|---|---|---|
| 0 | 1.3300 | 0.205 | 0 | 0 |
| 25 | 1.3310 | 0.206 | 103.00 | 3.55 |
| 50 | 1.3321 | 0.208 | 107.96 | 3.55 |
| 75 | 1.3332 | 0.211 | 116.05 | 3.55 |
| 100 | 1.3343 | 0.218 | 125.22 | 3.55 |
| 125 | 1.3353 | 0.213 | 120.57 | 3.55 |

**Table 6**
**Numerical robustness analysis sensitivity variation with fabrication parameter perturbations**

| Parameter varied | Perturbation | Computed sensitivity (°/RIU) | Change in sensitivity (ΔS) from nominal |
|---|---|---|---|
| Ag thickness (nominal 40 nm) | 38 nm (–2 nm) | 498 | –68 (–12.0%) |
| Ag thickness (nominal 40 nm) | 42 nm (+2 nm) | 481 | –85 (–15.0%) |
| ZnO thickness (nominal 6 nm) | 4 nm (–2 nm) | 562 | –4 (–0.7%) |
| ZnO thickness (nominal 6 nm) | 8 nm (+2 nm) | 570 | +4 (+0.7%) |
| ZnTe thickness (nominal 4 nm) | 3 nm (–1 nm) | 430 | –136 (–24.0%) |
| ZnTe thickness (nominal 4 nm) | 5 nm (+1 nm) | ~10 | –256 (–45.2%) |
| Ag RI (±5% in Im(n)) | 4.062i → 4.490i | ~560 → ~572 | ±10 (±1.8%) |

**Table 7**
**Comparative analysis with recently published numerical SPR biosensor studies**

| Structure | Metal/Thickness (nm) | $\lambda$ (nm) | Sensitivity (°/RIU) | FOM ($RIU^{-1}$) | LOD (ng/mL) | Refs. |
|---|---|---|---|---|---|---|
| $CaF_2$/Ag/$Si_3N_4$/Ni/BP | Ag/45 | 633 | 403.92 | – | – | [20] |
| BK7/Al/Ni/Si/BP | Al/38 | 633 | 480.00 | – | 25 | [1] |
| BK7/Ag/ZnTe/SiC/BP | Ag/50 | 633 | 480.46 | – | – | [11] |
| $CaF_2$/Ag/$TiO_2$/$PbTiO_3$ | Ag/54 | 1000 | 486.00 | – | – | [21] |
| $CaF_2$/ZnO/Ag/ZnTe (This work) | Ag/40 | 633 | 574.42 | 125 | 25* | – |

**Note:** The reported LOD corresponds to the minimum modeled concentration; thus, a true experimental LOD requires noise characterization and is not provided here.

spectroscopic ellipsometry (wavelength-dependent RI) and X-ray reflectivity (thicknesses); (iii) integration of the Powell lens divergence-beam head with the 3648-pixel CCD and 12-bit ADC followed by full noise characterization (dark noise, shot noise, source drift, and mechanical vibration) to quantify the experimentally achievable resolution versus the Section 3.7; (iv) covalent immobilization of anti-AFP antibodies on the ZnTe surface using established silane–EDC/NHS chemistry with characterization of coverage and orientation; and (v) calibration of the functionalized sensor against AFP-spiked buffer and serum in the 0–125 ng/mL clinical range to validate the bulk-RI–AFP mapping and determine the true experimental LOD. Completing stages (i)–(v) would convert the present numerical predictions into experimentally substantiated performance figures.

## 4. Conclusion

This study presents a comprehensive numerical optimization of a $CaF_2$/ZnO/Ag/ZnTe multilayer SPR sensor for RI sensitivity relevant to AFP detection, conducted through TMM simulations at $\lambda$ = 633 nm. The work is purely numerical; no experimental fabrication, functionalization, or biological measurements were performed.

The central contribution is a rigorous theoretical justification for a nonconventional optimal Ag thickness of 40 nm well below the traditional 45–55 nm range. Loss-balance analysis shows that the ZnO adhesion layer adds an equivalent effective optical path to the photon-tunneling barrier, while the ZnTe protective layer reduces the exit-side radiation damping rate; both shift the critical-coupling condition toward thinner Ag films. At Ag = 40 nm, ZnTe = 4 nm, and ZnO = 6 nm, the structure achieves near-critical coupling with 93.18% optical coupling efficiency versus only 48.96% at the conventional 50 nm thickness in the same multilayer context.

The optimized sensor predicts a maximum angular sensitivity of ~575.715°/RIU at the RI corresponding to 100 ng/mL AFP, FOM > 120 $RIU^{-1}$ within the AFP-relevant RI range, >93% optical coupling efficiency across the modeled AFP RI range, and a TDLR of $3.55 \times 10^{-10}$ RIU under ideal noise-free conditions. The TDLR in particular is an ideal lower bound, not an achievable system resolution. This numerical sensitivity outperforms recently published AFP-targeted SPR designs by approximately 20%.

The divergence-beam (Powell lens) interrogation architecture eliminates mechanical angular scanning, with resolution bounded by detector digitization rather than motor step angle, offering a significant theoretical resolution advantage over conventional motor-driven systems.

Future work will pursue the experimental validation steps, including fabrication of the $CaF_2$/ZnO/Ag/ZnTe stack, integration and noise characterization of the Powell lens, anti-AFP functionalization of the ZnTe surface, and calibration against AFP spiked buffer and serum. Experimental verification will be essential before any clinical or analytical performance claims can be made.

## Ethical Statement

This study does not contain any studies with human or animal subjects performed by any of the authors.

## Conflicts of Interest

The authors declare that they have no conflicts of interest to this work.

## Data Availability Statement

Data sharing is not applicable to this article as no new data were created or analyzed in this study.

## Author Contribution Statement

**Jordan H. Hossea:** Conceptualization, Methodology, Software, Writing – original draft, Supervision. **Athuman Mfinanga:** Validation, Formal analysis, Investigation, Data curation, Writing – review & editing, Visualization. **Vitalis Mwinyi:** Validation, Formal analysis, Resources, Data curation, Writing – review & editing, Visualization, Project administration.

## References

[1] Bahador, H., & Aliakbari, N. (2025). High-sensitivity plasmonic biosensor utilizing black phosphorus-silicon heterostructures for early detection of alpha-fetoprotein biomarker. *Plasmonics*, *20*(8), 6419–6426. https://doi.org/10.1007/s11468-025-02849-0

[2] Bray, F., Ferlay, J., Soerjomataram, I., Siegel, R. L., Torre, L. A., & Jemal, A. (2018). Global cancer statistics 2018: GLOBOCAN estimates of incidence and mortality worldwide for 36 cancers in 185 countries. *CA: A Cancer Journal for Clinicians*, *68*(6), 394–424. https://doi.org/10.3322/caac.21492

[3] Zhang, J., Chen, G., Zhang, P., Zhang, J., Li, X., Gan, D., . . . , & Ye, Y. (2020). The threshold of alpha-fetoprotein (AFP) for the diagnosis of hepatocellular carcinoma: A systematic review and meta-analysis. *PLOS One*, *15*(2), e0228857. https://doi.org/10.1371/journal.pone.0228857

[4] Olaniyan, M., Ajiboye, K., Ochagu, O. R., Olaniyan, T., Adeniran, M., Tijani, W., . . . , & Odegbemi, O. B. (2024). Alpha-fetoprotein as a predictor of liver disease progression in HBV patients with HIV and HCV co-infections. *Journal of Current Oncology and Medical Sciences*, *4*(3), 896–906. http://submission.journalofcoms.com/index.php/JCOMS/article/view/241

[5] Lyimo, E. P., Rumisha, S. F., Mremi, I. R., Mangu, C. D., Kishamawe, C., Chiduo, M. G., . . . , & Mboera, L. E. G. (2020). Cancer mortality patterns in tanzania: A retrospective hospital-based study, 2006–2015. *JCO Global Oncology*, *6*, 224–232. https://doi.org/10.1200/JGO.19.00270

[6] Qiang, Z., Yuan, R., Chai, Y., Wang, N., Zhuo, Y., Zhang, Y., & Li, X. (2006). A new potentiometric immunosensor for determination of $\alpha$-fetoprotein based on improved gelatin–silver complex film. *Electrochimica Acta*, *51*(18), 3763–3768. https://doi.org/10.1016/j.electacta.2005.10.039

[7] Jiao, Y., Du, C., Zong, L., Guo, X., Han, Y., Zhang, X., . . . , & Huang, W. (2020). 3D vertical-flow paper-based device for simultaneous detection of multiple cancer biomarkers by fluorescent immunoassay. *Sensors and Actuators B: Chemical*, *306*, 127239. https://doi.org/10.1016/j.snb.2019.127239

[8] Liang, G., Liu, S., Zou, G., & Zhang, X. (2012). Ultrasensitive immunoassay based on anodic near-infrared electrochemiluminescence from dual-stabilizer-capped cdte nanocrystals. *Analytical Chemistry*, *84*(24), 10645–10649. https://doi.org/10.1021/ac302236a

[9] Huang, X., Zhao, Y., Li, H., Xiao, R., Ma, B., Chen, J., . . . , & Lei, G. (2026). Screening and SPR-guided maturation of anti-ricin cyclononapeptide for high-sensitivity fluorescent LFA integrated with ultracompact handheld reader. *Talanta*, *309*, 130005. https://doi.org/10.1016/j.talanta.2026.130005

[10] Fattahi, Z., Khosroushahi, A. Y., & Hasanzadeh, M. (2020). Recent progress on developing of plasmon biosensing of tumor biomarkers: Efficient method towards early stage recognition of cancer. *Biomedicine & Pharmacotherapy*, *132*, 110850. https://doi.org/10.1016/j.biopha.2020.110850

[11] Vasimalla, Y., Chilukuri, S. S. M., Ben Khalifa, S., Chebaane, S., & Ghodhbani, R. (2025). A novel label-free plasmonic biosensor for afp detection employing zinc telluride and silicon carbide. *Plasmonics*, *20*(10), 8707–8718. https://doi.org/10.1007/s11468-025-02909-5

[12] Mondal, H. S., Ahmed, K. A., Birbilis, N., & Hossain, M. Z. (2023). Machine learning for detecting DNA attachment on SPR biosensor. *Scientific Reports*, *13*(1), 3742. https://doi.org/10.1038/s41598-023-29395-1

[13] Kukanskis, K., Elkind, J., Melendez, J., Murphy, T., Miller, G., & Garner, H. (1999). Detection of dna hybridization using the tispr-1 surface plasmon resonance biosensor. *Analytical Biochemistry*, *274*(1), 7–17. https://doi.org/10.1006/abio.1999.4241

[14] Yu, X.-Y., Qian, X.-D., & Xie, J. (2026). Theoretical analysis of the sensitivity limit for monolayer metal film based surface plasmon resonance sensor. *Optical and Quantum Electronics*, *58*(5), 217. https://doi.org/10.1007/s11082-026-08811-6

[15] Xu, Z., Hua, Y., Kong, X., Wu, H., Chang, J., Wan, B., . . . , & Cui, T. J. (2026). Band folding unlocks high-density hidden modes for sub-terahertz cancer cell phenotyping. *PhotoniX*, *7*(1), 9. https://doi.org/10.1186/s43074-026-00229-3

[16] Mustafizur Rahman, K., Nayan, F., Ahmed, R., & Rahman, M. (2025). Design and development of high sensitive surface plasmon resonance biosensors for glucose detection. *Plasmonics*, *20*(4), 2305–2319. https://doi.org/10.1007/s11468-024-02463-6

[17] Vasimalla, Y., & Singh, L. (2023). Design and analysis of planar waveguide-based SPR sensor for formalin detection using Ag-Chloride-BP structure. *IEEE Transactions on NanoBioscience*, *22*(2), 365–374. https://doi.org/10.1109/TNB.2022.3191971

[18] Karki, B., Uniyal, A., Sharma, T., Pal, A., & Srivastava, V. (2022). Indium phosphide and black phosphorus employed surface plasmon resonance sensor for formalin detection: Numerical analysis. *Optical Engineering*, *61*(1), 017101. https://doi.org/10.1117/1.OE.61.1.017101
[19] Rumi, R. B., Paul, A. K., Alyami, S. A., & Moni, M. A. (2024). Multi-disease detection using a prism-based surface plasmon resonance sensor: A TMM and FEM approach. *IEEE Transactions on NanoBioscience*, *23*(1), 51–62. https://doi.org/10.1109/TNB.2023.3286269
[20] Srivastava, S., Yadav, S., Mishra, A. C., Singh, S., Lohia, P., Dwivedi, D. K., . . . , & Hossain, M. K. (2024). Ultra-sensitive surface plasmon resonance biosensor for liver metastases and hepatocellular carcinoma detection using silicon nitride and black phosphorus nanomaterial. *Plasmonics*, *19*(2), 1031–1041. https://doi.org/10.1007/s11468-023-02059-6
[21] Jaiswal, L., Mishra, A. C., Yadav, S., Lohia, P., Dwivedi, D. K., Yadav, R. K., . . . , & Hossain, M. K. (2025). $TiO_2$ and $PbTiO_3$ assisted SPR biosensor for detection of malignancy in human-liver tissue with high sensitivity and figure of merit. *Journal of Computational Electronics*, *24*(1), 39. https://doi.org/10.1007/s10825-025-02277-7
[22] Akowuah, E. K., Gorman, T., & Haxha, S. (2009). Design and optimization of a novel surface plasmon resonance biosensor based on Otto configuration. *Optics Express*, *17*(26), 23511–23521. https://doi.org/10.1364/OE.17.023511
[23] Mohanty, B. C., & Kasiviswanathan, S. (2005). Two-prism setup for surface plasmon resonance studies. *Review of Scientific Instruments*, *76*(3), 033103. https://doi.org/10.1063/1.1865853
[24] Wang, C. (2019). A partial-dip observation mechanism for the resolution improvement of spectrum-like surface plasmon resonance waveforms. *IEEE Access*, *7*, 40516–40524. https://doi.org/10.1109/ACCESS.2019.2905600
[25] Johansen, K., Stålberg, R., Lundström, I., & Liedberg, B. (2000). Surface plasmon resonance: Instrumental resolution using photo diode arrays. *Measurement Science and Technology*, *11*(11), 1630–1638. https://doi.org/10.1088/0957-0233/11/11/313
[26] Phiri, I. K., & Zekriti, M. (2024). Sensitivity and performance enhancement of an SPR biosensor using a gold-silver alloy, zinc oxide and graphene. *Optical and Quantum Electronics*, *56*(8), 1332. https://doi.org/10.1007/s11082-024-07227-4
[27] Kumar, S., Yadav, A., & Malomed, B. A. (2023). High performance surface plasmon resonance based sensor using black phosphorus and magnesium oxide adhesion layer. *Frontiers in Materials*, *10*, 1131412. https://doi.org/10.3389/fmats.2023.1131412
[28] Hossea, J. (2025). Improving the interface roughness of the multilayer based on divergence beam surface plasmon resonance sensor using Whittaker filter. *Authorea.* https://doi.org/10.22541/au.176284458.85290706/v1
[29] Agarwal, S., Kumar, R., Pal, S., Prajapati, Y. K., & Saini, J. P. (2025). Magnesium fluoride and black phosphorus mediated long-range surface plasmon resonance biosensor for enhanced sensing of SARS-CoV-2 virus. *Journal of Optics*, *54*(3), 986–998. https://doi.org/10.1007/s12596-024-01772-7
[30] Bouandas, H., Slimani, Y., Ayadi, K., Ghebouli, M. A., Djemli, A., Fatmi, M., . . . , & Sillanpää, M. (2025). Sensitivity enhancement of biosensor (SPR) with $PtSe_2$ using Au-Si-Au thin films. *Journal of Optics*, *54*(3), 1043–1051. https://doi.org/10.1007/s12596-024-01807-z
[31] Panda, A., & Pukhrambam, P. D. (2022). Modeling of high-performance SPR refractive index sensor employing novel 2D materials for detection of malaria pathogens. *IEEE Transactions on NanoBioscience*, *21*(2), 312–319. https://doi.org/10.1109/TNB.2021.3115906
[32] Emon, W., Nayan, M. F., Salehin, S., Chaki, A., Tuba, S., & Ishtiak, K. M. (2024). Highly sensitive $ZnO/Ag/BaTiO_3$ $/MoS_2$ hybrid structure-based surface plasmon biosensor for the detection of mycobacterium tuberculosis bacteria. *Optics Continuum*, *3*(3), 495–512. https://doi.org/10.1364/OPTCON.518074
[33] Das, S., Prava Mondal, T., Kumar Roy, K., Reza Mahmud, R., Shariful Islam, M., & Barua, B. (2025). Design and optimization of an SPR-based biosensor with ultra-high sensitivity using a hybrid structure for accurate dengue virus detection. *Plasmonics*, *20*(11), 10243–10262. https://doi.org/10.1007/s11468-025-03107-z
[34] Utshob, Md. A. A. I., Juwel, M. B., Sabiha, R., Rahman, A., Safayat-Al, Imam., & Ishtiak, K. M. (2025). Design of a highly sensitive SPR biosensor for rapid malaria detection based on zinc telluride and blue phosphorus/tungsten disulfide material. *Biosensors and Bioelectronics: X*, *27*, 100709. https://doi.org/10.1016/j.biosx.2025.100709
[35] Rahman, M. M., Rana, M. M., Rahman, M. S., Anower, M. S., Mollah, M. A., & Paul, A. K. (2020). Sensitivity enhancement of SPR biosensors employing heterostructure of $PtSe_2$ and 2D materials. *Optical Materials*, *107*, 110123. https://doi.org/10.1016/j.optmat.2020.110123
[36] Karki, B., Ramya, K. C., Sandhya Devi, R. S., Srivastava, V., & Pal, A. (2022). Titanium dioxide, black phosphorus and bimetallic layer-based surface plasmon biosensor for formalin detection: Numerical analysis. *Optical and Quantum Electronics*, *54*(7), 451. https://doi.org/10.1007/s11082-022-03875-6
[37] Liu, L., Liu, Z., Zhang, Y., & Liu, S. (2022). Multi-channel optical fiber surface plasmon resonance sensor with narrow fwhm, high figure of merit, and wide detection range. *Plasmonics*, *17*(5), 2235–2244. https://doi.org/10.1007/s11468-022-01713-9
[38] Sun, L., Yang, Z., Ma, W., Wang, H., Zhang, B., Yan, S., & Ma, J. (2024). Dual-parameter fiber optic surface plasmon resonance sensor with narrow FWHM based on an incidence angle adjusting method. *Optics Express*, *32*(21), 37480–37491. https://doi.org/10.1364/OE.538596
[39] Singh, S., Singh, S., Singh, P. K., Yadav, R. K., Lohia, P., & Dwivedi, D. K. (2023). Theoretical study of malaria detection in blood samples using bimetal layer and zinc telluride nanomaterial-based surface plasmon resonance biosensor. *Plasmonics*, *18*(6), 2125–2136. https://doi.org/10.1007/s11468-023-01913-x
[40] Ashrafi, T. M. S., & Mohanty, G. (2025). Surface plasmon resonance sensors: A critical review of recent advances, market analysis, and future directions. *Plasmonics*, *20*(8), 6825–6845. https://doi.org/10.1007/s11468-024-02740-4

**How to Cite:** Hossea, J. H., Mfinanga, A., & Mwinyi, V. (2026). Numerical Optimization of a Divergence-Beam Surface Plasmon Resonance Sensor with $CaF_2/ZnO/Ag/ZnTe$ Multilayers for Alpha-Fetoprotein-Associated Refractive Index Sensing. *Journal of Optics and Photonics Research*. https://doi.org/10.47852/bonviewJOPR62028826